

High Curie temperature and high hole mobility in diluted magnetic semiconductors (B, Mn)X (X = N, P, As, Sb)

Xiang Li,¹ Jia-Wen Li,¹ Jing-Yang You,² Gang Su,^{1,3,4,5,*} and Bo Gu^{1,3,4,†}

¹*Kavli Institute for Theoretical Sciences, University of Chinese Academy of Sciences, Beijing 100049, China*

²*Department of Physics, National University of Singapore, 2 Science Drive 3, Singapore 117551*

³*CAS Center for Excellence in Topological Quantum Computation, University of Chinese Academy of Sciences, Beijing 100190, China*

⁴*Physical Science Laboratory, Huairou National Comprehensive Science Center, Beijing 101400, China*

⁵*School of Physical Sciences, University of Chinese Academy of Sciences, Beijing 100049, China*

(Dated: November 21, 2023)

Doping nonmagnetic semiconductors with magnetic impurities is a feasible way to obtain diluted magnetic semiconductors (DMSs). It is generally accepted that for the most extensively studied DMS, (Ga, Mn)As, its highest Curie temperature T_C was achieved at 200 K with a Mn concentration of approximately 16% in experiments. A recent experiment reported record-breaking high electron and hole mobilities in the semiconductor BAs [Science 377, 437 (2022)]. Since BAs shares the same zinc-blende structure with GaAs, here we predict four DMSs (B, Mn)X (X = N, P, As, Sb) by density functional theory calculations. Our results indicate that a significantly higher T_C in the range of 254 K to 300 K for (B, Mn)As with a Mn concentration of around 15.6%, and even higher T_C values above the room temperature for (B, Mn)N and (B, Mn)P with a Mn concentration exceeding 12.5%. Furthermore, we have predicted a large hole mobility of $1561 \text{ cm}^2 \text{ V}^{-1} \text{ s}^{-1}$ at 300 K for (B, Mn)As with a Mn concentration of about 3.7%, which is three orders of magnitude larger than the hole mobility of $4 \text{ cm}^2 \text{ V}^{-1} \text{ s}^{-1}$ at 300 K observed in the experiment for (Ga, Mn)As. Our findings predict the emergence of a new family of DMS, (B, Mn)X, and are expected to stimulate both experimental and theoretical studies of the DMS with high T_C and high mobilities.

I. INTRODUCTION

Magnetic semiconductors, owing to their combination of electron and spin degrees of freedom, hold significant promise for spintronic applications. One effective method to introduce long-range magnetic order and realize diluted magnetic semiconductor (DMS) is doping magnetic impurities such as Cr, Mn, Fe and Co in nonmagnetic semiconductors. Several efforts have focused on doping III-V zinc-blende semiconductors. In the case of the classic DMS (Ga, Mn)As, a Curie temperature T_C of 110 K was obtained with a Mn impurity concentration of 5.3% [1], and a higher T_C of 200 K was attained with a Mn impurity concentration of 16% by using non-equilibrium techniques [2]. However, further enhancing T_C of (Ga, Mn)As becomes challenging due to the valance mismatch of Mn^{2+} and Ga^{3+} . This leads Mn impurities to occupy interstitial positions as the doping concentration increases. [3–7]. In experiments of some Mn-doped III-V semiconductors, T_C was reported at 60 K for (Ga, Mn)P with a Mn concentration of 6% [8] and T_C reached 15 K in (Ga, Mn)Sb with a Mn concentration of 3.9% [9], as shown in TABLE I. It is noted that the carrier in DMSs (Ga, Mn)X (X = P, As, Sb) is hole, i.e. p-type. The ferromagnetism in (Ga, Mn)N remains a subject of debate, some experiments reported the room-temperature ferromagnetism [10–12] and attributed the high T_C to Mn_xN_y clusters instead of dopants [10, 11], while other experiments observed low T_C below 10 K [13–15].

TABLE I. Experimental results of Curie temperature, impurity concentration and carrier types for Mn-doped magnetic semiconductors (Ga, Mn)X (X = P, As, Sb) with zinc-blende structure.

Diluted magnetic semiconductors (years)	Curie temperature T_C	Impurity concentration	Carrier types
(Ga, Mn)P (2005) [8]	60 K	6%	p-type
(Ga, Mn)As (2011) [2]	200 K	16%	p-type
(Ga, Mn)Sb (2014) [9]	15 K	3.9%	p-type

Some DMSs with high T_C have been reported in experiments in the past decade [16]. A T_C of 230 K was obtained in p-type DMS (Ba, K)(Zn, Mn)₂As₂ with a Mn impurity concentration of 15% [17, 18]. This DMS has the advantage of decoupled charge and spin doping [19, 20]. The hole-mediated ferromagnetism in (Ba, K)(Zn, Mn)₂As₂ has been discussed in photoemission spectroscopy experiments [21, 22] and theoretical calculations [23, 24], similar to the picture discussed in (Ga, Mn)As. The T_C of 45 K in Co-doped n-type DMS Ba(Zn, Co)₂As₂ was also reported in the experiment [25]. Experiments have reported T_C of 340 K in (Ga, Fe)Sb with a Fe concentration of 25% [26] and T_C of 385 K in (In, Fe)Sb with Fe concentration of 35% [27]. The valence match between dopant Fe^{3+} and hosts Ga^{3+} and In^{3+} and the very high impurity concentration appear to be key factors contributing to these high T_C values [28]. T_C of Mn-doped $\text{Si}_{0.25}\text{Ge}_{0.75}$ with a Mn concentration of 5% was reported to be 280 K [29] and honeycomb structure (Zn, Co)O monolayer with a Co concentration of 11.1% was confirmed to exhibit long-range ferromagnetism with T_C above 300 K [30].

Intrinsic two-dimensional (2D) magnetic semiconductors

* gsu@ucas.ac.cn

† gubo@ucas.ac.cn

have also been synthesized successfully and studied in recent years. However, T_C of these 2D magnetic semiconductors in experiments, such as CrI_3 [31], $\text{Cr}_2\text{Ge}_2\text{Te}_6$ [32], CrCl_3 [33], CrBr_3 [34], Cr_2S_3 [35, 36], CrSBr [37] and CrSiTe_3 [38] are far below the room temperature. In order to enhance T_C of 2D magnetic semiconductors, effects of strain, electric field and heterostructure are theoretically studied, where some high T_C 2D magnetic semiconductors are proposed [39–49].

For the magnetic semiconductor, high mobility is also required for semiconductor applications. For the classic DMS (Ga, Mn)As with hole carriers, the experimental hole mobility of (Ga, Mn)As is lower than $4 \text{ cm}^2\text{V}^{-1}\text{s}^{-1}$ at room temperature [50, 51]. In fact, there are few magnetic semiconductors with both high T_C and high hole mobility in experiments [29]. Recently, it was discovered that the semiconductor boron arsenide (BAs), isostructural to the zinc-blende GaAs, has both high electron mobility and hole mobility $1600 \text{ cm}^2\text{V}^{-1}\text{s}^{-1}$ [52]. Although BAs had been synthesized several decades ago [53–56], some theoretical works have reported the wide gap, high electron and hole mobilities and high thermal conductivity [57–64], there have been several experiments reporting transports of the high electron mobility [65–67], the high hole mobility has not been confirmed until 2022 [52]. Inspired by the experimental high hole mobility in BAs and the similarity between semiconductors BAs and GaAs, is it possible to obtain the DMS of Mn-doped BAs with both high T_C and high mobility?

In this paper, we carry out calculations on the Mn-doped zinc-blende BX ($X = \text{N}, \text{P}, \text{As}, \text{Sb}$) with the density functional theory (DFT). Our results show a high T_C in the range of 254 K to 300 K in (B, Mn)As with a Mn concentration of 15.6%, higher than the T_C of 200 K in (Ga, Mn)As with a Mn concentration of 16% in experiment, which might be attributed to the shorter length of B-B bond in BAs. Mn impurities in BAs keep it a p-type semiconductor, and a high hole mobility of $1561 \text{ cm}^2\text{V}^{-1}\text{s}^{-1}$ at 300 K is found in (B, Mn)As with a Mn concentration of about 3.7%. Other DMSs (B, Mn)N, (B, Mn)P and (B, Mn)Sb are also explored, T_C values above the room temperature are predicted for (B, Mn)N and (B, Mn)P with a Mn concentration of above 12.5%, while low T_C is obtained in (B, Mn)Sb. We use two cases for calculations of exchange couplings and Curie temperatures, results obtained from two cases all support our findings on high T_C in DMS of (B, Mn)X family.

II. COMPUTATIONAL DETAILS

First-principles calculations in this work were performed with the projector augmented wave (PAW) method [68] based on the DFT as implemented in the Vienna ab initio simulation package (VASP) [69]. The choice of the electron exchange-correlation functional was generalized gradient approximation (GGA) with the form of Perdew-Burke-Ernzerhof (PBE) realization [70]. Lattice constants and atomic positions were fully relaxed until the maximum force acting on all atoms was less than $1 \times 10^{-4} \text{ eV}$ and the total energy was converged to $1 \times 10^{-8} \text{ eV}$ with the Gaussian smearing method. Calculations of

exchange coupling J_i were performed by using the $2 \times 2 \times 2$ conventional cubic supercell. The Monkhorst-Pack k-point mesh [71] of size $6 \times 6 \times 6$ was used for the Brillouin zone (BZ) sampling in structure optimization and self-consistent processes of exchange coupling calculations, while for calculations of band structures and mobilities using the primitive cell, the Monkhorst-Pack k-point mesh of size $9 \times 9 \times 9$ was used. The plane-wave cutoff energy was set to be 500 eV. The electron correlation of the 3d transition atom Mn was considered by using the DFT+U method introduced by Dudarev et al. [72]. Most of results were obtained with $U = 5 \text{ eV}$ and the effect of different values of U has been discussed.

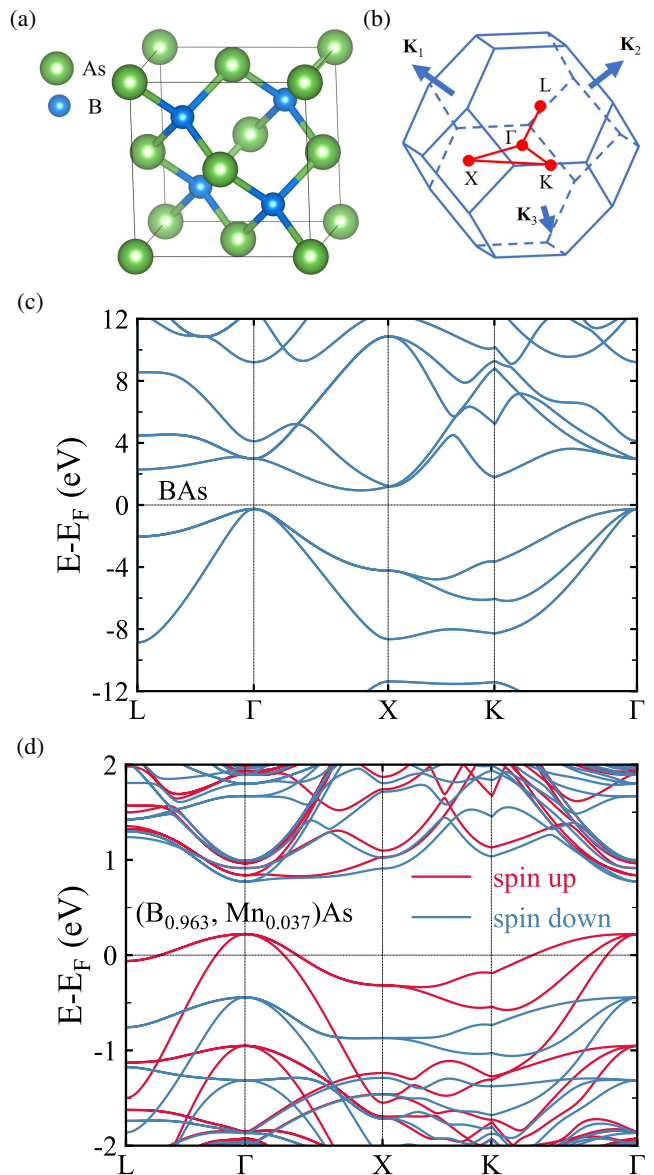


FIG. 1. (a) Zinc-blende crystal structure of the semiconductor BAs and (b) its first Brillouin zone. (c) Band structure of BAs with an indirect gap of 1.20 eV. (d) Band structure of the Mn-doped diluted magnetic semiconductor $(\text{B}_{0.963}, \text{Mn}_{0.037})\text{As}$ with a direct gap of 0.55 eV at Γ .

III. RESULTS

A. Exchange couplings of (B, Mn)As

Zinc-blende BAs has the space group $F\bar{4}3m$ (No. 216), its crystal structure and the first Brillouin zone with high symmetry paths indicated with red color are shown in FIG. 1(a) and FIG. 1(b), respectively. As shown in FIG. 1(c), BAs is a semiconductor with a calculated indirect gap of 1.20 eV, which is consistent with experimental values of 1.46 eV [53–56] and other calculations [57–61]. The $3 \times 3 \times 3$ primitive supercell with $B_{26}MnAs_{27}$ is adopted to study the electronic structure of the Mn-doped BAs. As shown in FIG. 1(d), $(B_{0.963}, Mn_{0.037})As$ is a p-type semiconductor and the band gap shrinks to 0.55 eV and becomes direct at Γ .

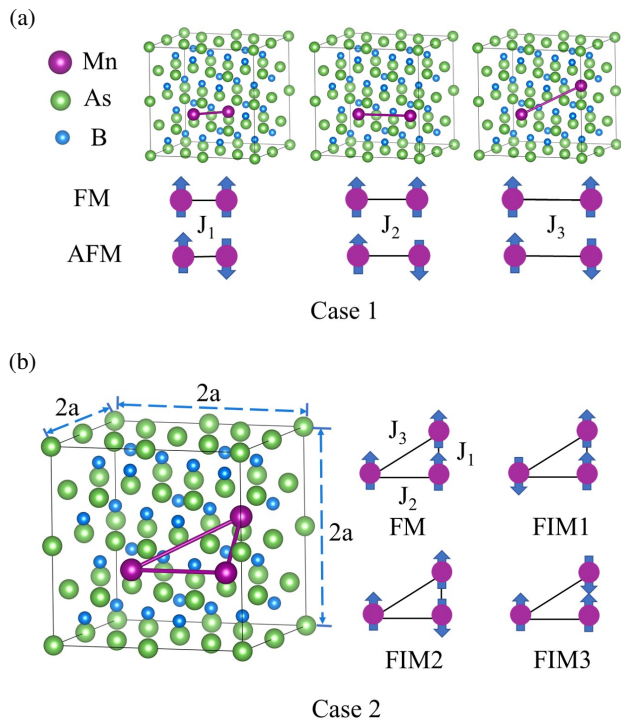


FIG. 2. Two different cases of constructing supercells to calculate the exchange coupling parameters between Mn impurities in semiconductor BAs. (a) Case 1: three different supercells of $B_{30}Mn_2As_{32}$ are used, where the nearest-neighbor exchange coupling J_1 , the next-nearest-neighbor exchange coupling J_2 and the third-nearest-neighbor exchange coupling J_3 are calculated independently. (b) Case 2: a supercell of $B_{29}Mn_3As_{32}$ is used, where exchange coupling parameters J_1 , J_2 and J_3 are calculated conjointly. See text for details.

In order to estimate T_C of the Mn-doped BAs, we should calculate the magnetic exchange coupling of two Mn impurities first. The disordered magnetic system is mapped to the classical Heisenberg-type Hamiltonian with J_1 , J_2 and J_3 denoting exchange couplings for the nearest neighbor, the next-nearest neighbor and the third-nearest neighbor between two impurity

sites, respectively, Hamiltonian is expressed as

$$H = - \sum_{i<j} J_1 \mathbf{S}_i \cdot \mathbf{S}_j - \sum_{i<k} J_2 \mathbf{S}_i \cdot \mathbf{S}_k - \sum_{i<l} J_3 \mathbf{S}_i \cdot \mathbf{S}_l \quad (1)$$

where two impurities are coupled ferromagnetically for conditions of $J_i > 0$ while antiferromagnetically for conditions of $J_i < 0$. In this work, exchange coupling parameters are calculated via two cases illustrated in FIG. 2. To avoid the influence of unphysical long-range exchange interaction from magnetic atoms in mirror neighbor cells and reduce the computation, some different $2 \times 2 \times 2$ cubic supercells are adopted as shown in FIG. 2, where a stands for the lattice constant of BAs.

TABLE II. Exchange coupling parameters J_i (meV) of two Mn impurities in (B, Mn)As and (Ga, Mn)As calculated by DFT+U with spin $S = 5/2$ and Hubbard correlation parameter $U = 5$ eV. J_1 , J_2 and J_3 denote the exchange coupling for the nearest neighbor, the second-nearest neighbor and the third-nearest neighbor, respectively.

		J_1 (meV)	J_2 (meV)	J_3 (meV)
Case 1	(B, Mn)As	15.813	1.226	2.215
	(Ga, Mn)As	10.215	0.136	1.811
Case 2	(B, Mn)As	12.527	-0.884	0.036
	(Ga, Mn)As	8.305	-0.633	0.808

For Case 1, three different supercells of $B_{30}Mn_2As_{32}$ are used. Ferromagnetic (FM) configuration with parallel spins and antiferromagnetic (AFM) configuration with anti-parallel spins structures are considered. Case 1 is the conventional way to construct supercells in past studies of DMSs [73–86]. J_1 , J_2 and J_3 are calculated independently. For J_1 , two impurities are located at $(0.375, 0.125, 0.375)2a$ and $(0.625, 0.375, 0.375)2a$ illustrated in FIG. 2(a) and their energy expressions are given by

$$\begin{aligned} E_{AFM} &= E_0 + J_1 S^2, \\ E_{FM} &= E_0 - J_1 S^2, \end{aligned} \quad (2)$$

where E_0 is the energy independent of spin configurations. The energy difference between FM and AFM configurations gives the J_1 . For J_2 , two impurities are located at $(0.375, 0.125, 0.375)2a$ and $(0.875, 0.125, 0.375)2a$ and their energy expressions are given by

$$\begin{aligned} E_{AFM} &= E_0 + 2J_2 S^2, \\ E_{FM} &= E_0 - 2J_2 S^2. \end{aligned} \quad (3)$$

J_2 can be calculated by Eq. (3) with DFT results of E_{AFM} and E_{FM} . For J_3 , two impurities are located at $(0.375, 0.125, 0.375)2a$ and $(0.875, 0.375, 0.625)2a$ and their energy expressions are given by

$$\begin{aligned} E_{AFM} &= E_0 + 2J_3 S^2, \\ E_{FM} &= E_0 - 2J_3 S^2. \end{aligned} \quad (4)$$

J_3 can be obtained by Eq. (4).

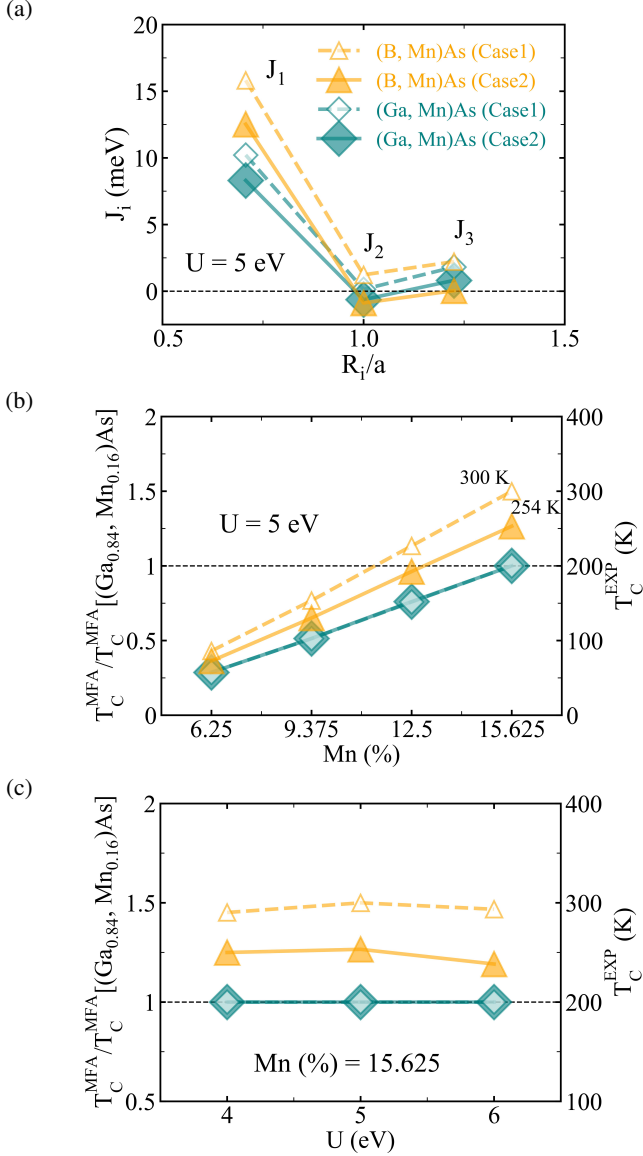


FIG. 3. Exchange coupling parameters J_i and Curie temperature T_C for Mn-doped BAs and GaAs. (a) Exchange coupling J_i as a function of distance R_i between two Mn impurities, where a is the lattice constant and Hubbard correlation parameter $U = 5$ eV. The same data in TABLE II. (b) Ratio of the Curie temperatures $T_C^{\text{MFA}}/T_C^{\text{MFA}}[(\text{Ga}_{0.84}, \text{Mn}_{0.16})\text{As}]$ with the mean-field approximation (MFA) by Eq. (6) as a function of Mn impurity concentration, where $U = 5$ eV. $T_C^{\text{MFA}}[(\text{Ga}_{0.84}, \text{Mn}_{0.16})\text{As}]$ corresponds to the $T_C^{\text{EXP}} = 200$ K of $(\text{Ga}_{0.84}, \text{Mn}_{0.16})\text{As}$ in experiment. Such correspondence is depicted by a black dashed line. (c) Ratio of Curie temperatures $T_C^{\text{MFA}}/T_C^{\text{MFA}}[(\text{Ga}_{0.84}, \text{Mn}_{0.16})\text{As}]$ as a function of parameter U , where Mn impurity concentration is fixed as 15.625%. The exchange couplings used in Eq. (6) is shown in Supplement Material [87].

For Case 2, a supercell of $\text{B}_{29}\text{Mn}_3\text{As}_{32}$ is used, where three Mn impurities are located at $(0.375, 0.125, 0.375)2a$, $(0.875,$

$0.125, 0.375)2a$ and $(0.875, 0.375, 0.625)2a$. J_1 , J_2 and J_3 are calculated conjointly. Bonds of impurity sites form a right triangle each line of which corresponds to different kind of exchange coupling as marked in the right panel of FIG. 2(b). Four different spin configurations including FM and three ferromagnetic configurations (FIM1, FIM2 and FIM3) are considered and their corresponding energy formulae are expressed as

$$\begin{aligned} E_{\text{FM}} &= E_0 - J_1 S^2 - 2J_2 S^2 - 2J_3 S^2, \\ E_{\text{FIM1}} &= E_0 - J_1 S^2 + 2J_2 S^2 + 2J_3 S^2, \\ E_{\text{FIM2}} &= E_0 + J_1 S^2 + 2J_2 S^2 - 2J_3 S^2, \\ E_{\text{FIM3}} &= E_0 + J_1 S^2 - 2J_2 S^2 + 2J_3 S^2. \end{aligned} \quad (5)$$

J_1 , J_2 and J_3 can be calculated by Eq. (5) with DFT results of E_{FM} , E_{FIM1} , E_{FIM2} and E_{FIM3} .

The obtained exchange coupling parameters J_1 , J_2 and J_3 for Mn-doped BAs and GaAs are shown in TABLE II and FIG. 3(a), where $U = 5$ eV. For Mn atom with five local d electrons, the spin is set to be $S = 5/2$. It is noted that obtained values of exchange couplings J_1 , J_2 and J_3 are independent of impurity concentrations, and the disorder effect due to impurities in DMS is included in coordination numbers in the mean-field formula of T_C in Eq. (6). Exchange couplings of (B, Mn)As and (Ga, Mn)As calculated by Case 1 and Case 2 show similar behaviors as a function of distance between two impurities R_i (in unit of the lattice constant a). The nearest coupling J_1 is ferromagnetic and dominates the exchange interaction. J_i drops drastically when two impurities are placed more distant. The strength of J_1 is near ten times larger than J_2 which is weak-antiferromagnetic for Case 2 while is weak-ferromagnetic for Case 1. The third-nearest coupling J_3 rises slightly and is much smaller than the nearest coupling J_1 . Both J_2 and J_3 close to zero. J_1 of (B, Mn)As is much larger than that of (Ga, Mn)As for both cases, which might be attributed to the shorter B-B bond length in BAs and thus shorter Mn-Mn distance in (B, Mn)As.

B. Curie temperatures of (B, Mn)As

Curie temperature T_C is estimated via Weiss mean-field formula

$$T_C^{\text{MFA}} = \frac{2}{3k_B} S(S+1) \sum_i \sum_{\alpha} Z_i^{\alpha} P_{\alpha} J_i. \quad (6)$$

Z_i^{α} is the coordination number of one doping configuration α for the given doping concentration, P_{α} is the probability of this doping configuration. Doping configurations α are generated via Disorder code [88, 89]. To simulate the doped system with random distribution of magnetic impurities, different doping configurations for a given doping concentration are considered in the $2 \times 2 \times 2$ cubic supercell with $\text{B}_{32}\text{As}_{32}$. The condition of the doping concentration 6.25% is given as an example where two B atoms in the supercell $\text{B}_{32}\text{As}_{32}$ are replaced with Mn impurities, so there are three inequivalent doping configurations and their corresponding Z_i^{α} and P_{α} are listed in TABLE III, see Supplemental Material for more details about this

method and coordination numbers of other doping concentrations [87].

TABLE III. For doping concentration 6.25%, doping configuration α , coordination number Z_i^α of the exchange coupling J_i , and probability P_α .

α	Z_i^α for Mn1	Z_i^α for Mn2	P_α
1	{1, 0, 0}	{1, 0, 0}	4/9
2	{0, 2, 0}	{0, 2, 0}	1/9
3	{0, 0, 2}	{0, 0, 2}	4/9

Values of T_C^{MFA} , calculated by Eq. (6) with exchange couplings listed in TABLE II, are far beyond the experimental value T_C^{EXP} , because it is expected that the mean-field formula always overestimates the Curie temperature. In order to provide a more reliable estimation of Curie temperatures of (Ga, Mn)As and (B, Mn)As, we analyze our data in the following way. As shown in FIG. 3(b), the ratio of the mean-field Curie temperatures $T_C^{\text{MFA}}/T_C^{\text{MFA}}[(\text{Ga}_{0.84}, \text{Mn}_{0.16})\text{As}]$ as a function of Mn impurity concentration is plotted, where $U = 5$ eV. The T_C^{MFA} of $(\text{Ga}_{0.84}, \text{Mn}_{0.16})\text{As}$ is taken as the unit one, which physically corresponds to the $T_C^{\text{EXP}} = 200$ K of $(\text{Ga}_{0.84}, \text{Mn}_{0.16})\text{As}$ in the experiment [2]. We plot such correspondence in FIG. 3(b) by a black dashed line. In this way, it is shown that T_C^{MFA} of (B, Mn)As is larger than that of (Ga, Mn)As for both Case 1 and Case 2, while the ratios $T_C^{\text{MFA}}/T_C^{\text{MFA}}[(\text{Ga}_{0.84}, \text{Mn}_{0.16})\text{As}]$ of (Ga, Mn)As of Case 1 and Case 2 are overlapped. $T_C^{\text{MFA}}/T_C^{\text{MFA}}[(\text{Ga}_{0.84}, \text{Mn}_{0.16})\text{As}]$ is 1.27 for (B, Mn)As with a Mn concentration of 15.625% for Case 2, which corresponds to $T_C^{\text{EXP}} = 254$ K for (B, Mn)As with a Mn concentration of 15.625%. $T_C^{\text{MFA}}/T_C^{\text{MFA}}[(\text{Ga}_{0.84}, \text{Mn}_{0.16})\text{As}]$ is 1.50 for (B, Mn)As with 15.625% of Mn for Case 1, which corresponds to $T_C^{\text{EXP}} = 300$ K for (B, Mn)As with 15.625% of Mn. A high Curie temperature T_C^{EXP} is predicted for (B, Mn)As with a Mn concentration around 15.625%, larger than experimental value of Curie temperature T_C^{EXP} of 200 K for (Ga, Mn)As with a Mn concentration of 16% [2]. For (B, Mn)As with reasonable U values of Mn impurities, $T_C^{\text{MFA}}/T_C^{\text{MFA}}[(\text{Ga}_{0.84}, \text{Mn}_{0.16})\text{As}]$ with a Mn concentration around 15.625% is calculated as shown in FIG. 3(c). Results of exchange couplings with $U = 4$ eV and $U = 6$ eV are listed in Supplemental Material [87]. $T_C^{\text{MFA}}/T_C^{\text{MFA}}[(\text{Ga}_{0.84}, \text{Mn}_{0.16})\text{As}]$ changes slightly for both Case 1 and Case 2 when varying parameter U . More results of Case 2 and $U = 5$ eV will be discussed in the following part.

C. Curie temperatures of (B, Mn)X (X = N, P, Sb)

In order to verify the reliability of the above rescaling method, the ratio of the mean-field Curie temperature $T_C^{\text{MFA}}/T_C^{\text{MFA}}[(\text{Ga}_{0.84}, \text{Mn}_{0.16})\text{As}]$ as a function of the Mn impurity concentration for (Ga, Mn)P and (Ga, Mn)Sb are calculated and shown in FIG. 4(a) with exchange couplings of Case 2. Experimental Curie temperatures of (Ga, Mn)P, (Ga, Mn)As and (Ga, Mn)Sb from TABLE I are labeled by hollow

squares. Ultra low T_C^{EXP} is found in (Ga, Mn)Sb and T_C^{EXP} of 84 K is obtained for (Ga, Mn)P with a Mn concentration of 6% by our rescaling method, which are consistent with experiments [8, 9]. Curie temperatures of possible DMSs (B, Mn)X with X = N, P, Sb are also calculated in the same way. Band structures of (B, Mn)N, (B, Mn)P and (B, Mn)Sb suggest that they are all p-type semiconductors as shown in Supplemental Material [87]. FIG. 4(b) predicts high T_C values above room temperature for (B, Mn)N and (B, Mn)P when the Mn concentration is above 12.5%, and low T_C for (B, Mn)Sb. Similar results are obtained for Case 1 with $U = 5$ eV as shown in Supplemental Material [87].

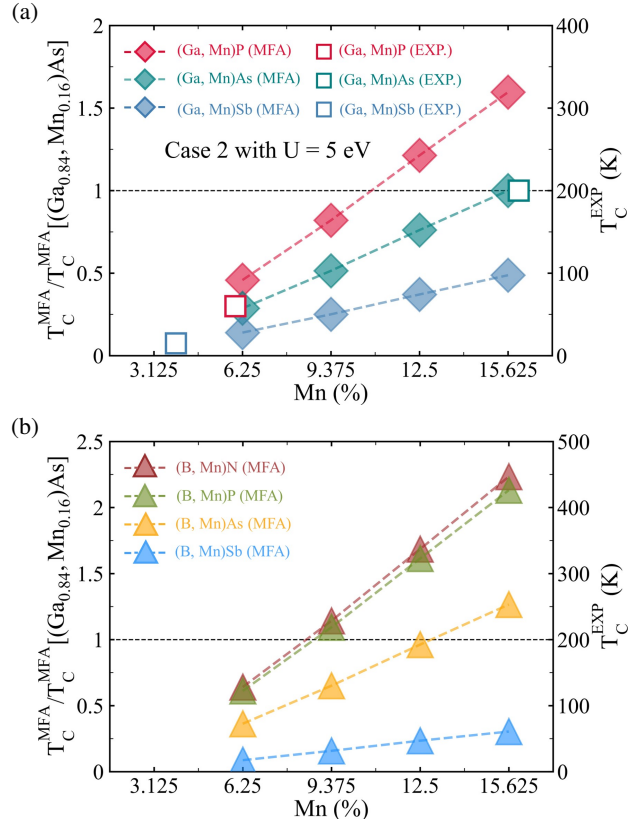


FIG. 4. The ratio of the mean-field Curie temperature $T_C^{\text{MFA}}/T_C^{\text{MFA}}[(\text{Ga}_{0.84}, \text{Mn}_{0.16})\text{As}]$ as a function of Mn impurity concentration for (a) Mn-doped GaX (X = P, As, Sb), and (b) Mn-doped BX (X = N, P, As, Sb). Case 2 with $U = 5$ eV is considered. $T_C^{\text{MFA}}/T_C^{\text{MFA}}[(\text{Ga}_{0.84}, \text{Mn}_{0.16})\text{As}] = 1$ corresponds to T_C^{EXP} of 200 K of $(\text{Ga}_{0.84}, \text{Mn}_{0.16})\text{As}$ in experiment. Such correspondence is depicted by a black dashed line in (a) and (b).

D. Hole mobility of (B, Mn)As

We estimate the hole mobility of BAs, GaAs and (B, Mn)As by deformation potential (DP) theory. The DP theory was proposed by Bardeen and Shockley [90] in 1950s to describe the charge transport in non-polar semiconductors. The mobility formula of the three-dimensional (3D) semiconductor is de-

rived as

$$\mu_{3D} = \frac{2\sqrt{2\pi}eC_{3D}\hbar^4}{3(k_B T)^{3/2}E^2 m^{*5/2}}, \quad (7)$$

where $e > 0$ is the charge of the electron, \hbar is the reduced Planck constant, k_B is the Boltzmann constant, C_{3D} is the elastic constant or Young's modulus for 3D system, E is DP constant and m^* is the effective mass at the band edge. Due to the isotropy of the zinc-blende BAs and $(B_{0.963}, Mn_{0.037})As$, only transports along the z -axis are calculated, this direction corresponds to the Γ -X path in the Brillouin zone and only transports of the heavy hole are considered.

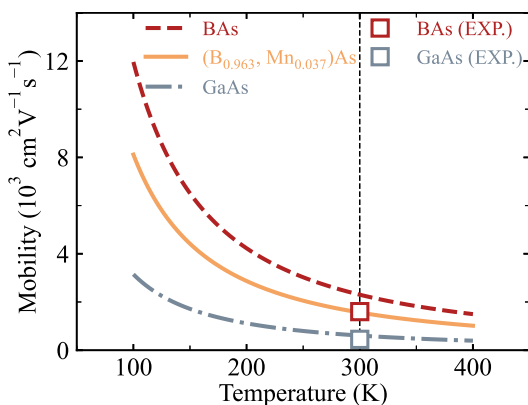


FIG. 5. Calculated hole mobilities of BAs, $(B_{0.963}, Mn_{0.037})As$ and GaAs by using deformation potential theory. Experimental values of BAs and GaAs at 300 K listed in TABLE IV are illustrated by squares.

Calculated results are listed in TABLE IV and FIG. 5 depicts the calculated mobility versus the temperature, where experimental values of BAs and GaAs at 300 K listed in TABLE IV are added by hollow squares. It is shown that the calculated mobilities for BAs and GaAs at 300 K are consistent with experimental values. The estimated hole mobility of $(B_{0.963}, Mn_{0.037})As$ is $1561 \text{ cm}^2\text{V}^{-1}\text{s}^{-1}$ at 300 K which is three orders of magnitude larger than the mobility of $4 \text{ cm}^2\text{V}^{-1}\text{s}^{-1}$ at 300 K for $(Ga, Mn)As$.

TABLE IV. The calculated Young's modulus C_{3D} (GPa), deformation potential constant E_h (eV), effective heavy hole mass m_h (m_0) where m_0 is the mass of the bare electron, and heavy hole mobility μ_h ($\text{cm}^2\text{V}^{-1}\text{s}^{-1}$) at 300 K for BAs, $(B_{0.963}, Mn_{0.037})As$, and GaAs. For comparison, experimental values of μ_h are also shown.

	C_{3D} (GPa)	E_h (eV)	m_h (m_0)	μ_h ($\text{cm}^2\text{V}^{-1}\text{s}^{-1}$)	μ_h (EXP.)
BAs	240.78	4.93	0.59	2301	1600 [52]
$(B, Mn)As$	192.74	4.78	0.64	1561	
GaAs	74.71	2.81	0.98	605	450 [91]
$(Ga, Mn)As$					≤ 4 [50, 51]

IV. CONCLUSION

By using the density functional theory, we have studied the Mn-doped zinc-blende semiconductors $(B, Mn)X$ ($X = N, P, As, Sb$). Our calculations show that Mn impurities introduce ferromagnetism in these semiconductors. By the rescaling method of the calculated Curie temperature, we predict a high T_C in the range of 254 K to 300 K for $(B, Mn)As$ with 15.6% Mn impurities, which is higher than the highest T_C of 200 K for $(Ga, Mn)As$ with 16% Mn impurities in the experiment. T_C values above the room temperature are predicted for $(B, Mn)N$ and $(B, Mn)P$ with a Mn concentration of above 12.5%. By the deformation potential theory, $(B_{0.963}, Mn_{0.037})As$ is found to have high hole mobility $1561 \text{ cm}^2\text{V}^{-1}\text{s}^{-1}$ at 300 K which is three orders of magnitude larger than the hole mobility of $(Ga, Mn)As$ in the experiment. Our results highlight the new DMS $(B, Mn)As$ with high T_C and high mobilities.

V. ACKNOWLEDGEMENTS

This work is supported by National Key R&D Program of China (Grant No. 2022YFA1405100), National Natural Science Foundation of China (Grant No. 12074378), Chinese Academy of Sciences Project for Young Scientists in Basic Research (Grant No. YSBR-030), National Natural Science Foundation of China (Grant No. 11834014), Basic Research Program of the Chinese Academy of Sciences Based on Major Scientific Infrastructures (Contract No. JZHKYPT-2021-08), Beijing Municipal Science and Technology Commission (Grant No. Z191100007219013), and Strategic Priority Research Program of Chinese Academy of Sciences (Grants No. XDB28000000 and No. XDB33000000).

[1] H. Ohno, Making Nonmagnetic Semiconductors Ferromagnetic, *Science* **281**, 951 (1998).
 [2] L. Chen, X. Yang, F. Yang, J. Zhao, J. Misuraca, P. Xiong, and S. von Molnár, Enhancing the Curie Temperature of Ferromagnetic Semiconductor $(Ga, Mn)As$ to 200 K via Nanostructure Engineering, *Nano Lett.* **11**, 2584 (2011).

[3] T. Jungwirth, J. Sinova, J. Mašek, J. Kučera, and A. H. MacDonald, Theory of ferromagnetic $(III, Mn)V$ semiconductors, *Rev. Mod. Phys.* **78**, 809 (2006).
 [4] T. Dietl, A ten-year perspective on dilute magnetic semiconductors and oxides, *Nat. Mater.* **9**, 965 (2010).
 [5] H. Ohno, A window on the future of spintronics, *Nat. Mater.* **9**, 952 (2010).

- [6] K. Sato, L. Bergqvist, J. Kudrnovský, P. H. Dederichs, O. Eriksson, I. Turek, B. Sanyal, G. Bouzerar, H. Katayama-Yoshida, V. A. Dinh, T. Fukushima, H. Kizaki, and R. Zeller, First-principles theory of dilute magnetic semiconductors, *Rev. Mod. Phys.* **82**, 1633 (2010).
- [7] T. Dietl and H. Ohno, Dilute ferromagnetic semiconductors: Physics and spintronic structures, *Rev. Mod. Phys.* **86**, 187 (2014).
- [8] M. A. Scarpulla, B. L. Cardozo, R. Farshchi, W. M. H. Oo, M. D. McCluskey, K. M. Yu, and O. D. Dubon, Ferromagnetism in $\text{Ga}_{1-x}\text{Mn}_x\text{P}$: Evidence for Inter-Mn Exchange Mediated by Localized Holes within a Detached Impurity Band, *Phys. Rev. Lett.* **95**, 207204 (2005).
- [9] M.-Y. Zhu, J. Lu, J.-L. Ma, L.-X. Li, H.-L. Wang, D. Pan, and J.-H. Zhao, Molecular-beam epitaxy of high-quality diluted magnetic semiconductor (Ga, Mn)Sb single-crystalline films, *Acta Phys. Sin.* **64**, 077501 (2015).
- [10] M. Sawicki, T. Dietl, C. T. Foxon, S. V. Novikov, R. P. Campion, K. W. Edmonds, K. Y. Wang, A. D. Giddings, and B. L. Gallagher, Search For Hole Mediated Ferromagnetism In Cubic (Ga,Mn)N, *AIP Conf. Proc.* **772**, 1371 (2005).
- [11] S. V. Novikov, K. W. Edmonds, L. X. Zhao, A. D. Giddings, K. Y. Wang, R. P. Campion, C. R. Staddon, M. W. Fay, Y. Han, P. D. Brown, M. Sawicki, B. L. Gallagher, and C. T. Foxon, Mn doping and p-type conductivity in zinc-blende GaMnN layers grown by molecular beam epitaxy, *J. Vac. Sci. Technol. B* **23**, 1294 (2005).
- [12] V. A. Chitta, J. A. H. Coaquira, J. R. L. Fernandez, C. A. Duarte, J. R. Leite, D. Schikora, D. J. As, K. Lischka, and E. Abramof, Room temperature ferromagnetism in cubic GaN epilayers implanted with Mn^+ ions, *Appl. Phys. Lett.* **85**, 3777 (2004).
- [13] S. Stefanowicz, G. Kunert, C. Simserides, J. A. Majewski, W. Stefanowicz, C. Kruse, S. Figge, T. Li, R. Jakiela, K. N. Trohidou, A. Bonanni, D. Hommel, M. Sawicki, and T. Dietl, Phase diagram and critical behavior of the random ferromagnet $\text{Ga}_{1-x}\text{Mn}_x\text{N}$, *Phys. Rev. B* **88**, 081201 (2013).
- [14] A. A. Freeman, K. W. Edmonds, N. R. S. Farley, S. V. Novikov, R. P. Campion, C. T. Foxon, B. L. Gallagher, E. Sarigiannidou, and G. van der Laan, Depth dependence of the Mn valence and Mn-Mn coupling in (Ga,Mn)N, *Phys. Rev. B* **76**, 081201 (2007).
- [15] L. Janicki, G. Kunert, M. Sawicki, E. Piskorska-Hommel, K. Gas, R. Jakiela, D. Hommel, and R. Kudrawiec, Fermi level and bands offsets determination in insulating (Ga,Mn)N/GaN structures, *Sci. Rep.* **7**, 41877 (2017).
- [16] Z. Sun, N. Tang, S. Chen, F. Zhang, H. Fan, S. Zhang, R. Wang, X. Lin, J. Liu, W. Ge, and B. Shen, Spin injection into heavily-doped n-GaN via Schottky barrier, *J. Semicond.* **44**, 082501 (2023).
- [17] K. Zhao, B. Chen, G. Zhao, Z. Yuan, Q. Liu, Z. Deng, J. Zhu, and C. Jin, Ferromagnetism at 230 K in $(\text{Ba}_{0.7}\text{K}_{0.3})(\text{Zn}_{0.85}\text{Mn}_{0.15})_2\text{As}_2$ diluted magnetic semiconductor, *Chin. Sci. Bull.* **59**, 2524 (2014).
- [18] K. Zhao, Z. Deng, X. C. Wang, W. Han, J. L. Zhu, X. Li, Q. Q. Liu, R. C. Yu, T. Goko, B. Frandsen, L. Liu, F. Ning, Y. J. Uemura, H. Dabkowska, G. M. Luke, H. Luetkens, E. Morenzoni, S. R. Dunsiger, A. Senyshyn, P. Böni, and C. Q. Jin, New diluted ferromagnetic semiconductor with Curie temperature up to 180 K and isostructural to the '122' iron-based superconductors, *Nat. Commun.* **4**, 1442 (2013).
- [19] J. Dong, X. Zhao, L. Fu, Y. Gu, R. Zhang, Q. Yang, L. Xie, and F. Ning, (Ca,K)(Zn,Mn) $_2$ As $_2$: Ferromagnetic semiconductor induced by decoupled charge and spin doping in CaZn_2As_2 , *J. Semicond.* **43**, 072501 (2022).
- [20] X. Zhao, J. Dong, L. Fu, Y. Gu, R. Zhang, Q. Yang, L. Xie, Y. Tang, and F. Ning, $(\text{Ba}_{1-x}\text{Na}_x)\text{F}(\text{Zn}_{1-x}\text{Mn}_x)\text{Sb}$: A novel fluoride-antimonide magnetic semiconductor with decoupled charge and spin doping, *J. Semicond.* **43**, 112501 (2022).
- [21] H. Suzuki, K. Zhao, G. Shibata, Y. Takahashi, S. Sakamoto, K. Yoshimatsu, B. J. Chen, H. Kumigashira, F. H. Chang, H. J. Lin, D. J. Huang, C. T. Chen, B. Gu, S. Maekawa, Y. J. Uemura, C. Q. Jin, and A. Fujimori, Photoemission and X-ray absorption studies of the isostructural to Fe-based superconductors diluted magnetic semiconductor $\text{Ba}_{1-x}\text{K}_x(\text{Zn}_{1-y}\text{Mn}_y)_2\text{As}_2$, *Phys. Rev. B* **91**, 140401 (2015).
- [22] H. Suzuki, G. Q. Zhao, K. Zhao, B. J. Chen, M. Horio, K. Koshiishi, J. Xu, M. Kobayashi, M. Minohara, E. Sakai, K. Horiba, H. Kumigashira, B. Gu, S. Maekawa, Y. J. Uemura, C. Q. Jin, and A. Fujimori, Fermi surfaces and p-d hybridization in the diluted magnetic semiconductor $\text{Ba}_{1-x}\text{K}_x(\text{Zn}_{1-y}\text{Mn}_y)_2\text{As}_2$ studied by soft X-ray angle-resolved photoemission spectroscopy, *Phys. Rev. B* **92**, 235120 (2015).
- [23] J. K. Glasbrenner, I. Žutić, and I. I. Mazin, Theory of Mn-doped II-II-V semiconductors, *Phys. Rev. B* **90**, 140403 (2014).
- [24] B. Gu and S. Maekawa, Diluted magnetic semiconductors with narrow band gaps, *Phys. Rev. B* **94**, 155202 (2016).
- [25] S. Guo, H. Man, K. Wang, C. Ding, Y. Zhao, L. Fu, Y. Gu, G. Zhi, B. A. Frandsen, S. C. Cheung, Z. Guguchia, K. Yamakawa, B. Chen, H. Wang, Z. Deng, C. Q. Jin, Y. J. Uemura, and F. Ning, $\text{Ba}(\text{Zn},\text{Co})_2\text{As}_2$: A diluted ferromagnetic semiconductor with n-type carriers and isostructural to 122 iron-based superconductors, *Phys. Rev. B* **99**, 155201 (2019).
- [26] N. T. Tu, P. N. Hai, L. D. Anh, and M. Tanaka, High-temperature ferromagnetism in heavily Fe-doped ferromagnetic semiconductor (Ga,Fe)Sb, *Appl. Phys. Lett.* **108**, 192401 (2016).
- [27] N. T. Tu, P. N. Hai, L. D. Anh, and M. Tanaka, Heavily Fe-doped ferromagnetic semiconductor (In,Fe)Sb with high Curie temperature and large magnetic anisotropy, *Appl. Phys. Express* **12**, 103004 (2019).
- [28] J.-Y. You, B. Gu, S. Maekawa, and G. Su, Microscopic mechanism of high-temperature ferromagnetism in Fe, Mn, and Cr-doped InSb, InAs, and GaSb magnetic semiconductors, *Phys. Rev. B* **102**, 094432 (2020).
- [29] H. Wang, S. Sun, J. Lu, J. Xu, X. Lv, Y. Peng, X. Zhang, Y. Wang, and G. Xiang, High Curie Temperature Ferromagnetism and High Hole Mobility in Tensile Strained Mn-Doped SiGe Thin Films, *Adv. Funct. Mater.* **30**, 2002513 (2020).
- [30] R. Chen, F. Luo, Y. Liu, Y. Song, Y. Dong, S. Wu, J. Cao, F. Yang, A. N'Diaye, P. Shafer, Y. Liu, S. Lou, J. Huang, X. Chen, Z. Fang, Q. Wang, D. Jin, R. Cheng, H. Yuan, R. J. Birgeneau, and J. Yao, Tunable room-temperature ferromagnetism in Co-doped two-dimensional van der Waals ZnO, *Nat. Commun.* **12**, 3952 (2021).
- [31] B. Huang, G. Clark, E. Navarro-Moratalla, D. R. Klein, R. Cheng, K. L. Seyler, D. Zhong, E. Schmidgall, M. A. McGuire, D. H. Cobden, W. Yao, D. Xiao, P. Jarillo-Herrero, and X. Xu, Layer-dependent ferromagnetism in a van der Waals crystal down to the monolayer limit, *Nature* **546**, 270 (2017).
- [32] C. Gong, L. Li, Z. Li, H. Ji, A. Stern, Y. Xia, T. Cao, W. Bao, C. Wang, Y. Wang, Z. Q. Qiu, R. J. Cava, S. G. Louie, J. Xia, and X. Zhang, Discovery of intrinsic ferromagnetism in two-dimensional van der Waals crystals, *Nature* **546**, 265 (2017).
- [33] X. Cai, T. Song, N. P. Wilson, G. Clark, M. He, X. Zhang, T. Taniguchi, K. Watanabe, W. Yao, D. Xiao, M. A. McGuire, D. H. Cobden, and X. Xu, Atomically Thin CrCl_3 : An In-Plane Layered Antiferromagnetic Insulator, *Nano Lett.* **19**, 3993 (2019).

- [34] Z. Zhang, J. Shang, C. Jiang, A. Rasmita, W. Gao, and T. Yu, Direct Photoluminescence Probing of Ferromagnetism in Monolayer Two-Dimensional CrBr_3 , *Nano Lett.* **19**, 3138 (2019).
- [35] F. Cui, X. Zhao, J. Xu, B. Tang, Q. Shang, J. Shi, Y. Huan, J. Liao, Q. Chen, Y. Hou, Q. Zhang, S. J. Pennycook, and Y. Zhang, Controlled Growth and Thickness-Dependent Conduction-Type Transition of 2D Ferrimagnetic Cr_2S_3 Semiconductors, *Adv. Mater.* **32**, 1905896 (2020).
- [36] J. Chu, Y. Zhang, Y. Wen, R. Qiao, C. Wu, P. He, L. Yin, R. Cheng, F. Wang, Z. Wang, J. Xiong, Y. Li, and J. He, Submillimeter-Scale Growth of One-Unit-Cell-Thick Ferrimagnetic Cr_2S_3 Nanosheets, *Nano Lett.* **19**, 2154 (2019).
- [37] K. Lee, A. H. Dismukes, E. J. Telford, R. A. Wisconsin, J. Wang, X. Xu, C. Nuckolls, C. R. Dean, X. Roy, and X. Zhu, Magnetic Order and Symmetry in the 2D Semiconductor CrSb , *Nano Lett.* **21**, 3511 (2021).
- [38] B. Achinuq, R. Fujita, W. Xia, Y. Guo, P. Bencok, G. van der Laan, and T. Hesjedal, Covalent Mixing in the 2D Ferromagnet CrSiTe_3 Evidenced by Magnetic X-Ray Circular Dichroism, *Phys. Status Solidi RRL* **16**, 2100566 (2022).
- [39] L. Webster and J.-A. Yan, Strain-tunable magnetic anisotropy in monolayer CrCl_3 , CrBr_3 , and CrI_3 , *Phys. Rev. B* **98**, 144411 (2018).
- [40] J.-Y. You, Z. Zhang, B. Gu, and G. Su, Two-Dimensional Room-Temperature Ferromagnetic Semiconductors with Quantum Anomalous Hall Effect, *Phys. Rev. Appl.* **12**, 024063 (2019).
- [41] X.-J. Dong, J.-Y. You, B. Gu, and G. Su, Strain-Induced Room-Temperature Ferromagnetic Semiconductors with Large Anomalous Hall Conductivity in Two-Dimensional $\text{Cr}_2\text{Ge}_2\text{Se}_6$, *Phys. Rev. Appl.* **12**, 014020 (2019).
- [42] X.-J. Dong, J.-Y. You, Z. Zhang, B. Gu, and G. Su, Great enhancement of Curie temperature and magnetic anisotropy in two-dimensional van der Waals magnetic semiconductor heterostructures, *Phys. Rev. B* **102**, 144443 (2020).
- [43] J.-Y. You, X.-J. Dong, B. Gu, and G. Su, Electric field induced topological phase transition and large enhancements of spin-orbit coupling and Curie temperature in two-dimensional ferromagnetic semiconductors, *Phys. Rev. B* **103**, 104403 (2021).
- [44] X. Jiang, Q. Liu, J. Xing, N. Liu, Y. Guo, Z. Liu, and J. Zhao, Recent progress on 2D magnets: Fundamental mechanism, structural design and modification, *Appl. Phys. Rev.* **8**, 031305 (2021).
- [45] J.-Y. You, X.-J. Dong, B. Gu, and G. Su, Possible Room-Temperature Ferromagnetic Semiconductors, *Chin. Phys. Lett.* **40**, 067502 (2023).
- [46] J.-W. Li, Z. Zhang, J.-Y. You, B. Gu, and G. Su, Two-dimensional Heisenberg model with material-dependent superexchange interactions, *Phys. Rev. B* **107**, 224411 (2023).
- [47] D. Wei, The room temperature ferromagnetism in highly strained two-dimensional magnetic semiconductors Semiconductors, *J. Semicond.* **44**, 040401 (2023).
- [48] J.-Y. You, B. Gu, and G. Su, The p-orbital magnetic topological states on a square lattice, *Natl. Sci. Rev.* **9**, nwab114 (2022).
- [49] D. Zhao, C. Zhang, C. Zhang, W. Ji, S. Li, and P. Wang, Magnetic tuning in a novel half-metallic Ir_2Te_2 monolayer, *J. Semicond.* **43**, 052001 (2022).
- [50] W. Limmer, M. Glunk, S. Mascheck, A. Koeder, D. Klarer, W. Schoch, K. Thonke, R. Sauer, and A. Waag, Coupled plasmon-LO-phonon modes in $\text{Ga}_{1-x}\text{Mn}_x\text{As}$, *Phys. Rev. B* **66**, 205209 (2002).
- [51] W. Limmer, A. Koeder, S. Frank, V. Avrutin, W. Schoch, R. Sauer, K. Zuern, J. Eisenmenger, P. Ziemann, E. Peiner, and A. Waag, Effect of annealing on the depth profile of hole concentration in $(\text{Ga},\text{Mn})\text{As}$, *Phys. Rev. B* **71**, 205213 (2005).
- [52] J. Shin, G. A. Gamage, Z. Ding, K. Chen, F. Tian, X. Qian, J. Zhou, H. Lee, J. Zhou, L. Shi, T. Nguyen, F. Han, M. Li, D. Broido, A. Schmidt, Z. Ren, and G. Chen, High ambipolar mobility in cubic boron arsenide, *Science* **377**, 437 (2022).
- [53] J. A. Perri, S. La Placa, and B. Post, New group III-group V compounds: BP and BAs, *Acta Cryst.* **11**, 310 (1958).
- [54] S. M. Ku, Preparation and Properties of Boron Arsenides and Boron Arsenide-Gallium Arsenide Mixed Crystals, *J. Electrochem. Soc.* **113**, 813 (1966).
- [55] T. L. Chu and A. E. Hyslop, Preparation and Properties of Boron Arsenide Films, *J. Electrochem. Soc.* **121**, 412 (1974).
- [56] S. Wang, S. F. Swingle, H. Ye, F.-R. F. Fan, A. H. Cowley, and A. J. Bard, Synthesis and Characterization of a p-Type Boron Arsenide Photoelectrode, *J. Am. Chem. Soc.* **134**, 11056 (2012).
- [57] I. H. Nwigboji, Y. Malozovsky, L. Franklin, and D. Bagayoko, Calculated electronic, transport, and related properties of zinc blende boron arsenide (zb-BAs), *J. Appl. Phys.* **120**, 145701 (2016).
- [58] M. P. Surh, S. G. Louie, and M. L. Cohen, Quasiparticle energies for cubic BN, BP, and BAs, *Phys. Rev. B* **43**, 9126 (1991).
- [59] D. A. Broido, L. Lindsay, and T. L. Reinecke, Ab initio study of the unusual thermal transport properties of boron arsenide and related materials, *Phys. Rev. B* **88**, 214303 (2013).
- [60] S. Chae, K. Mengle, J. T. Heron, and E. Kioupakis, Point defects and dopants of boron arsenide from first-principles calculations: Donor compensation and doping asymmetry, *Appl. Phys. Lett.* **113**, 212101 (2018).
- [61] K. Bushick, K. Mengle, N. Sanders, and E. Kioupakis, Band structure and carrier effective masses of boron arsenide: Effects of quasiparticle and spin-orbit coupling corrections, *Appl. Phys. Lett.* **114**, 022101 (2019).
- [62] T.-H. Liu, B. Song, L. Meroueh, Z. Ding, Q. Song, J. Zhou, M. Li, and G. Chen, Simultaneously high electron and hole mobilities in cubic boron-V compounds: BP, BAs, and BSb, *Phys. Rev. B* **98**, 081203 (2018).
- [63] L. Lindsay, D. A. Broido, and T. L. Reinecke, First-Principles Determination of Ultrahigh Thermal Conductivity of Boron Arsenide: A Competitor for Diamond?, *Phys. Rev. Lett.* **111**, 025901 (2013).
- [64] T. Feng, L. Lindsay, and X. Ruan, Four-phonon scattering significantly reduces intrinsic thermal conductivity of solids, *Phys. Rev. B* **96**, 161201 (2017).
- [65] J. S. Kang, M. Li, H. Wu, H. Nguyen, and Y. Hu, Experimental observation of high thermal conductivity in boron arsenide, *Science* **361**, 575 (2018).
- [66] F. Tian, B. Song, X. Chen, N. K. Ravichandran, Y. Lv, K. Chen, S. Sullivan, J. Kim, Y. Zhou, T.-H. Liu, M. Goni, Z. Ding, J. Sun, G. A. G. Udalamatta Gamage, H. Sun, H. Ziyace, S. Huyan, L. Deng, J. Zhou, A. J. Schmidt, S. Chen, C.-W. Chu, P. Y. Huang, D. Broido, L. Shi, G. Chen, and Z. Ren, Unusual high thermal conductivity in boron arsenide bulk crystals, *Science* **361**, 582 (2018).
- [67] S. Li, Q. Zheng, Y. Lv, X. Liu, X. Wang, P. Y. Huang, D. G. Cahill, and B. Lv, High thermal conductivity in cubic boron arsenide crystals, *Science* **361**, 579 (2018).
- [68] P. E. Blöchl, Projector augmented-wave method, *Phys. Rev. B* **50**, 17953 (1994).
- [69] G. Kresse and J. Furthmüller, Efficient iterative schemes for ab initio total-energy calculations using a plane-wave basis set, *Phys. Rev. B* **54**, 11169 (1996).
- [70] J. P. Perdew, K. Burke, and M. Ernzerhof, Generalized Gradient Approximation Made Simple, *Phys. Rev. Lett.* **77**, 3865 (1996).

- [71] H. J. Monkhorst and J. D. Pack, Special points for Brillouin-zone integrations, *Phys. Rev. B* **13**, 5188 (1976).
- [72] S. L. Dudarev, G. A. Botton, S. Y. Savrasov, C. J. Humphreys, and A. P. Sutton, Electron-energy-loss spectra and the structural stability of nickel oxide: An LSDA+U study, *Phys. Rev. B* **57**, 1505 (1998).
- [73] P. Mahadevan and A. Zunger, First-principles investigation of the assumptions underlying model-Hamiltonian approaches to ferromagnetism of 3d impurities in III-V semiconductors, *Phys. Rev. B* **69**, 115211 (2004).
- [74] P. Mahadevan, A. Zunger, and D. D. Sarma, Unusual Directional Dependence of Exchange Energies in GaAs Diluted with Mn: Is the RKKY Description Relevant?, *Phys. Rev. Lett.* **93**, 177201 (2004).
- [75] E. Kulatov, H. Nakayama, H. Mariette, H. Ohta, and Y. A. Uspenskii, Electronic structure, magnetic ordering, and optical properties of GaN and GaAs doped with Mn, *Phys. Rev. B* **66**, 045203 (2002).
- [76] S. Sanvito, P. Ordejón, and N. A. Hill, First-principles study of the origin and nature of ferromagnetism in $\text{Ga}_{1-x}\text{Mn}_x\text{As}$, *Phys. Rev. B* **63**, 165206 (2001).
- [77] M. Jain, L. Kronik, J. R. Chelikowsky, and V. V. Godlevsky, Electronic structure and spin polarization of Mn-containing dilute magnetic III-V semiconductors, *Phys. Rev. B* **64**, 245205 (2001).
- [78] F. Máca and J. Mašek, Electronic states in $\text{Ga}_{1-x}\text{Mn}_x\text{As}$: Substitutional versus interstitial position of Mn, *Phys. Rev. B* **65**, 235209 (2002).
- [79] M. v. Schilfgaarde and O. N. Mryasov, Anomalous exchange interactions in III-V dilute magnetic semiconductors, *Phys. Rev. B* **63**, 233205 (2001).
- [80] Y. C. Cheng, Z. Y. Zhu, W. B. Mi, Z. B. Guo, and U. Schwingenschlögl, Prediction of two-dimensional diluted magnetic semiconductors: Doped monolayer MoS_2 systems, *Phys. Rev. B* **87**, 100401 (2013).
- [81] A. Ramasubramaniam and D. Naveh, Mn-doped monolayer MoS_2 : An atomically thin dilute magnetic semiconductor, *Phys. Rev. B* **87**, 195201 (2013).
- [82] R. Mishra, W. Zhou, S. J. Pennycook, S. T. Pantelides, and J.-C. Idrobo, Long-range ferromagnetic ordering in manganese-doped two-dimensional dichalcogenides, *Phys. Rev. B* **88**, 144409 (2013).
- [83] L. Seixas, A. Carvalho, and A. H. Castro Neto, Atomically thin dilute magnetism in Co-doped phosphorene, *Phys. Rev. B* **91**, 155138 (2015).
- [84] L. Sun, W. Zhou, Y. Liang, L. Liu, and P. Wu, Magnetic properties in Fe-doped SnS_2 : Density functional calculations, *Comput. Mater. Sci.* **117**, 489 (2016).
- [85] B. Li, T. Xing, M. Zhong, L. Huang, N. Lei, J. Zhang, J. Li, and Z. Wei, A two-dimensional Fe-doped SnS_2 magnetic semiconductor, *Nat. Commun.* **8**, 1958 (2017).
- [86] M. Huang, Z. Zheng, Z. Dai, X. Guo, S. Wang, L. Jiang, J. Wei, and S. Chen, DASP: Defect and Dopant ab-initio Simulation Package, *J. Semicond.* **43**, 042101 (2022).
- [87] See Supplemental Material at [URL will be inserted by publisher] for additional calculations results., .
- [88] J.-C. Lian, H.-Y. Wu, W.-Q. Huang, W. Hu, and G.-F. Huang, Algorithm for generating irreducible site-occupancy configurations, *Phys. Rev. B* **102**, 134209 (2020).
- [89] J.-C. Lian, Y. Si, T. Huang, W.-Q. Huang, W. Hu, and G.-F. Huang, Highly efficient tree search algorithm for irreducible site-occupancy configurations, *Phys. Rev. B* **105**, 014201 (2022).
- [90] J. Bardeen and W. Shockley, Deformation Potentials and Mobilities in Non-Polar Crystals, *Phys. Rev.* **80**, 72 (1950).
- [91] M. Sotoodeh, A. H. Khalid, and A. A. Rezazadeh, Empirical low-field mobility model for III-V compounds applicable in device simulation codes, *J. Appl. Phys.* **87**, 2890 (2000).